Article

Investigation on the coalescence of filaments in FFF process for high performance material (PEKK-A) for varying nozzle diameters and chamber temperatures

Antoine Runacher [1,2] *, Thomas Joffre [1], Germain Fauny [1], Claudia Salvan[1], Nils Marchal [1] and Francisco Chinesta [2]

1   Centre Technique Innovation Plasturgie et Composites, 2 rue Pierre et Marie Curie, 01100 Bellignat, France
2   Ecole Nationale des Arts et Métiers, Laboratoire PIMM, 151 Boulevard de l'hôpital, 75013 Paris, France
*   Correspondence: antoine.runacher@ensam.eu

Abstract: The use of Fused Filament Fabrication (FFF) of high-performance polymers is becoming increasingly prevalent, leading to the exploration of new applications. The use of such materials in critical cases for aerospace applications necessitates the verification of industry standards, particularly with regard to the requirements for part porosity. The authors investigate the effect of nozzle diameter and cooling temperature printing parameters on the porosity of the part by using existing modelling methods based on the sintering of cylinders and spheres and comparing the results to microscope snapshots of sections of parts. The models are able to be used as limits for predicting the longitudinal neck growth of the part. The value of the cooling temperature of the print has a minimal effect on the outcome while nozzle diameter and layer thickness have a strong impact on mesostructures.

1. Introduction

Since its birth in the 1960s, Additive Manufacturing (AM) methods have been rapidly developing. While not as efficient as traditional subtractive and formative methods, the quick design to part time and the customization possibilities of AM has contributed to its development, first for prototyping endeavors and now even for structural uses of parts [1].

A large number of such methods were developed over the years, for metals and polymer materials, each having their own drawbacks and perks. This multitude of methods result in the rapid increase of scientific publications regarding this set of methods, also contributing to the expansion of the field [2].

One of such fabrication process is the Fused Filament Fabrication (FFF) [3]. By feeding a polymer through a heating nozzle, a melted filament of material is extruded following a specific path [4]. Adjacent filaments will fuse to form a solid ensemble after the cooling of the material [5]. Successive layers of material deposited on top of each other will then form a finished part. This process can be applied to a wide array of materials [6][7][8], to produce parts of complex geometry, without molds or welds. It is however slower than traditional manufacturing, the manufactured part are also limited in size, and their mechanical properties are often worse than parts fabricated with the injection process [9]. This manufacturing process is described in figure 1.

There exists a market for FFF manufactured parts : while the manufacturing times are high, there is no added costs of molds. For a low volume of parts, these characteristics can be more advantageous than injection or welding. This is particularly the case in the aviation industry, as the parts made using FFF are lighter than their aluminium counterparts used in planes today and boast of a very low excess material consumption. Still, the high safety requirements of critical use parts need to be addressed [10].

To satisfy this drive for FFF processed parts in primary aerospace structures and its stringent safety requirements, of which the first is the need for fire resistant, not to produce
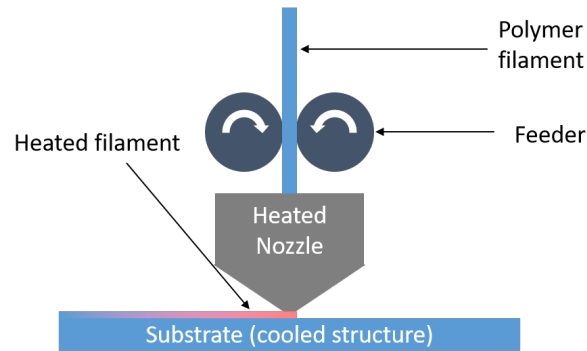
Figure 1. Fused Filament Fabrication process.

smoke when burnt material, that the fumes produced be safe for users and to have a high melting temperature. The second is to keep part porosity below 2% [11].

The PAEK familly of thermoplastic materials (PAEK, PEKK, PEEK, ...) complies with the specified safety regulations, but are notoriously hard to use in Fused Filament Fabrication [12], requiring a heated chamber for the coalescence between filament to occur. By increasing this temperature, the capillary time during which the coalescence takes place is longer, resulting in higher part strength [13].

During the deposition process, two adjacent beads of material are placed in intimate contact with each other. The high temperature of printing starts the bond formation process between filaments. It is the fusing of polymer chains at a molecular scale. When the cooling step of the process is finished, the healing of the part is characterized by the interdiffusion of polymer chains, from one bead to the next [14].

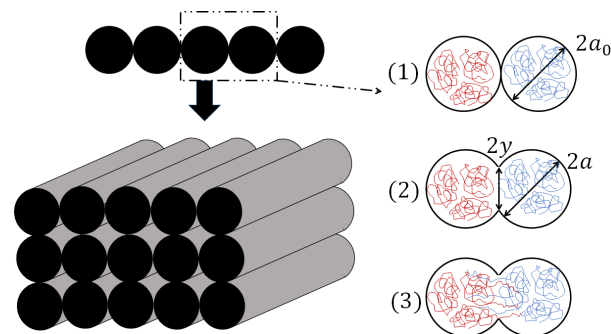This adhesion mechanism is shown in figure 2 .

Figure 2. Bond formation process between two filaments: (1) surface contacting; (2) neck growth; (3) molecular diffusion at interface and randomization, inspired from [15]

This coalescence is of varying degree when looking at a finished part, causing interrogations regarding the structural soundness of the part, hence the safety requirement on part porosity.

This phenomena was first modelled by Frenkel and Eshelby in 1945 and 1949 [16]. Describing the coalescence of two spherical beads of material modelled as a incompressible and viscous Newtonian fluid, in isothermal conditions, with an uniform stress tensor. This problem was solved with a small angle approximation.

Pokluda et al, in 1997 [17], expended the Frenkel-Eshelby model for all angles with a Runge-Kuta numerical method to solve the differential heat equation. This model provides a dimensionless solution of the neck growth for a bead of PLA. From this, the expected porosity should not vary with a change in radius of the considered beads.

As shown by Bakrari Balani[18], the surface tension of the material changes during the cooling process, and so does the viscosity. An accurate characterization of both is needed to model the behaviour of the porosity of a printed part.

Lepoivre et al, in 2021 [19], characterized the evolution of the surface tension and viscosity of PEKK with regards to the temperature and then used a numerical model to describe the evolution of the degree of coalescence with varying surface tension and viscosity. Their findings are used to accurately calculate the surface tension and viscosity of the PEKK for the presented model.

In 2023, Jiang et al. [20] investigated the coalescence of PLA in FFF by modelling the behavior of the coalescence and testing the results on printed filaments of varying sizes, but the long diameter of the filaments studied was limited to a nozzle diameter of 0.4 mm.

There is a need to determine the behaviour of larger filaments, for the increase in cooling time of the filaments gets higher with each increment in diameter. The effects of the chamber temperature, parameter with a sure impact on part young modulus, are not often seen in the literature [21].

In this publication, a framework based on Jiang et al.'s investigations, with Lepoivre et al.'s data on viscosity and surface tension of PEKK, explores the neck growth of PEKK filaments. This study will show the impact of nozzle diameter and cooling temperature on the longitudinal neck growth between filaments. The authors have not fund other examples in the literature of similar studies for the considered nozzle diameter.

These investigations on the neck growth will also be conducted in different chamber temperatures to quantify the effect of the parameter on the porosity of the part.

2. Materials and Methods

This section pertains to the methodology used to analyse section cuts of printed PEKK test pieces.

2.1. Modelling of the temperature of the bead

The cooling of a single filament is simplified to a one-dimensional transient heat transfer model. This method works under the assumption of a uniform temperature distribution throughout the cross section of the deposited filament [16]. The nozzle moves at a constant speed v. The temperature of the substrate is considered constant throughout the deposition and cooling process, from which the conduction of heat between layers is considered a convection. The figure 3 shows the energy interaction on a finite element dx of a heated filament.

$$h'(P - S)(T - T_\infty)dx$$

(Chamber)

$$\dot{q}_{x+dx}$$

$$dx$$

$$\rho CA \frac{\partial T}{\partial t} dx$$
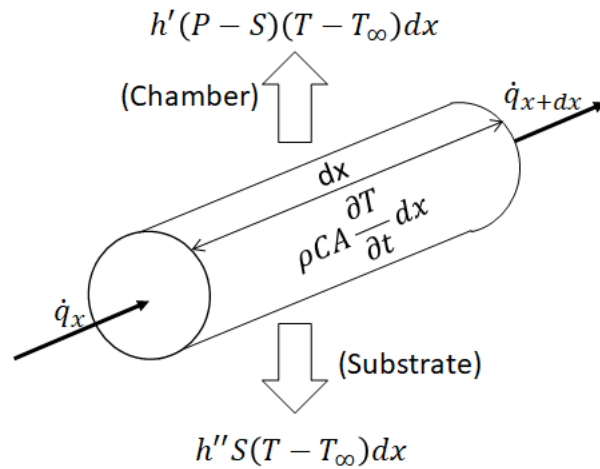
$$\dot{q}_x$$

(Substrate)

$$h''S(T - T_\infty)dx$$

Figure 3. Energy interaction on finite element dx, inspired from [22]

From this the heat differential equation of the system can be written.

$$\rho C A \frac{\partial T}{\partial t} = A \frac{\partial(k \frac{\partial T}{\partial x})}{\partial x} - h(T - T_\infty) \tag{1}$$

With $T = T_0$ at $x = 0$, $t \geq 0$ and $T = T_\infty$ at $x = \infty$ and $t \geq 0$, with C specific heat coefficient, ρ the density, A the cross section area of the filament, k the heat conductivity coefficient and h the convection coefficient of the system.

The coefficient h governs the effects of both heat convection with air and conduction with the substrate.

The nozzle is moving at a velocity v and $x = vt$. The time dependent term $\frac{\partial T}{\partial t}$ can be rewritten as

$$\frac{\partial T}{\partial t} = \frac{\partial T}{\partial x} \frac{\partial x}{\partial t} = \frac{\partial T}{\partial x} v \tag{2}$$

The previous equation becomes then :

$$\rho C A v \frac{\partial T}{\partial x} = A \frac{\partial(k \frac{\partial T}{\partial x})}{\partial x} - h(T - T_\infty) \tag{3}$$

And has for solution :

$$T(x) = T_\infty + (T_0 - T_\infty)e^{-mx} \tag{4}$$

With $m = \frac{\sqrt{1+4\alpha\beta}-1}{2\alpha}$, $x = vt$, $\alpha = \frac{k}{\rho C v}$, $\beta = \frac{hP}{\rho C v A}$

With $P = \pi(a + b)\left(\frac{64-3\lambda^4}{64-16\lambda^2}\right)$ and $A = \pi ab$ with a the major axis and b the minor axis of the cross-section of the deposited filament, considered elliptic, and where $\lambda = \frac{a-b}{a+b}$.

2.2. Modelling of coalescence between two beads of material

The porosity of the part is related to the sintering of two adjacent deposited filaments. The polymer filaments are printed at a temperature higher than the glass transition temperature. At those temperature, the polymer is considered as a Newtonian fluid.

Polychronopoulos and Vlachopoulos [23], in 2020, studied the role of heating and cooling in the sintering of both spheres and cylinders for Additive Manufacturing, detailing the steps to solve the coalescence problem of Fused Filament Fabrication.

The sintering process or coalescence is illustrated in figure 4.

The sintering is the behaviour that two adjacent liquid beads follow to form one unique bead of a longer radius. It is a phenomena that is dependent on the surface tension of the fluid, Γ, and the viscosity of the fluid η. The sintering process occurs until the temperature of the material crosses below the glass transition temperature as highlighted in the previous section. The material is then considered solid and will not be subject to further deformations related to the sintering of the beads. The sintering process is modeled from the dynamic equilibrium between the work of the surface tension forces and the work of the viscosity forces in the given fluid.

In the following sections, the equations leading to the expression of the evolution of the half angle of coalescence θ are reported. It is obtained under the form of a differential equation.

From θ, geometry relations between quantities give the theoretical longitudinal neck growth, the quantity of interest.
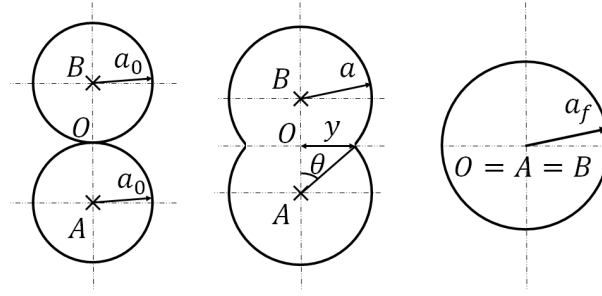
2.2.1. Sintering of Spheres

Figure 4. Sintering process of two cylinders or two spheres, inspired from [23]

If two spheres of radius a_0 intersect in one point of contact, they will gradually coalesce into one sphere of radius a_f with $a_f = a_0 \sqrt[3]{2}$ with that point of contact as the center of the newly formed sphere.

As shown in figure 4, at a given time t, the values of the radius of the bead $a(t)$, the half angle of coalescence $\theta(t)$, and the longitudinal neck growth $x(t)$ will be referred to as a, θ and x respectively in the following.

Pokluda et al. [17] establishes a framework to model the behaviour of the sintering of beads. The radius a of the beads is given by the conservation of the mass of the polymer, with the density of a bead constant with the temperature.

$$a = a_0 \left(\frac{4}{[1 + \cos \theta]^2 [2 - \cos \theta]} \right)^{1/3} \tag{5}$$

The area of a section S of two beads at a given time is given by equation 6 .

$$S = 4\pi a^2 [1 + \cos \theta] \tag{6}$$

The flow of material for spherical beads sintering is given by a biaxial extensional flow field. This leads to, solving the dynamic equilibrium between work of viscous forces and surface tension, the expression of a differential equation θ, the half angle of coalescence of the beads.

Polychronopoulos et al. [23], show the steps to the solution, and the expressions of the quantities of interest θ, the half angle of coalescence, and y, the longitudinal neck growth between filaments as follows. The differential equation in θ is solved using a Runge-Kuta algorithm with an initial value of θ, $\theta_0 = 0.01$ to avoid numerical instabilities.

$$\dot{\theta} = \frac{\Gamma}{a_0 \eta} \frac{2^{-5/3} \cos \theta \sin \theta (2 - \cos \theta)^{1/3}}{(1 - \cos \theta)(1 + \cos \theta)^{1/3}} \tag{7}$$

Finally, for spherical sintering, the longitudinal neck growth y is given by :

$$y = a_0 \sin \theta \left(\frac{4}{(1 + \cos \theta)^2 (2 - \cos \theta)} \right)^{1/3} \tag{8}$$

In the following sections, the half angle of coalescence and the longitudinal neck growth for spherical beads of material will respectively be noted θ_{sph} and y_{sph}

2.2.2. Sintering of Cylinders

In the case of fused filament fabrication, the sintering process may also be modeled as two elliptic cylinders fusing, which can be characterized by two circular cylinders of an unique radius $r_0 = b^2/a$ [24], with a the semi-major axis and b the semi-minor axis of the ellipse as described in the figure 5. The ultimate result of such coalescence is an unique cylinder, of the temperature of the polymer is maintained high enough for the sintering to continue. The variation in length of the cylinder will be ignored as it is negligible before
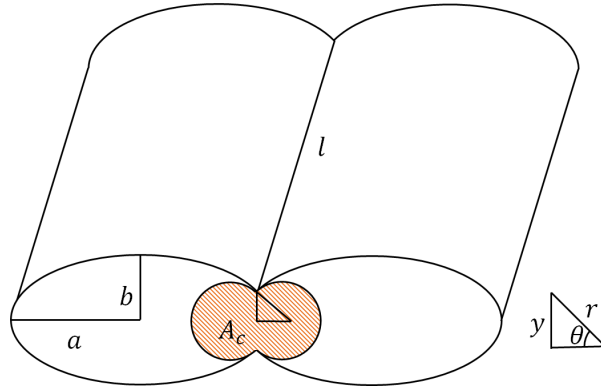
Figure 5. Diagram of Bonding, inspired from [24]

the variation in radius of the cylinder. For ease of comprehension and for the rest of the section, the functions $r(t)$, the radius of the two cylinders, $\theta(t)$ the half angle of coalescence as shown in the figure 5, $y(t)$ the longitudinal neck growth of the process, will be referred to as , r, θ , and y respectively.

The area of a circular segment of a disk formed by the section of two cylinders is as follows [25] and is shown in figure 6 where R is the radius, Θ the central angle in radians equal to 2θ, c the cord length, s the arc length, h the sagitta, d the apothem and A_{seg} the area of the segment (orange area in figure 6):

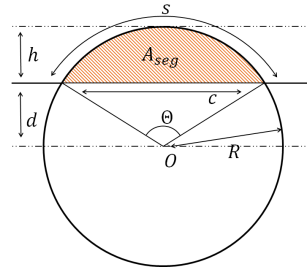**Figure 6.** Area of a segment of a circle

$$A_{seg} = \frac{R^2}{2}(\Theta - \sin\Theta) = R^2(\theta - \cos\theta\sin\theta) \tag{9}$$

From which, the area of the section of two cylinders during the sintering process A_c shown in orange in 5 is given by :

$$A_c = 2(A - A_{seg}) = 2\pi r^2 - 2r^2(\theta - \cos\theta\sin\theta) = 2r^2(\pi - \theta + \cos\theta\sin\theta) \tag{10}$$

From the conservation of mass between the steps of the sintering, the radius r of the circular cylinder is given [23]:

$$r = \frac{\sqrt{\pi}r_0}{\sqrt{\pi - \theta + \cos\theta\sin\theta}} \tag{11}$$

where $r_0 = \frac{b^2}{a}$ and θ is the half angle of coalescence as shown in figure 5.

From the given expressions of nominal radius r and area A_c and the dynamic equilibrium between the work of viscous forces and the surface tension, a differential equation with the half angle of coalescence θ is given.

The flow of material induced by the viscous forces and the surface tension of the fluid is a planar extensional flow when the sintering process is approaching the sintering of

cylinders, meaning that the work of viscous forces is expressed as a function of the strain rate of the system. By definition, the strain rate and the velocity of the deformation are linked, and so the dynamic equilibrium between viscous forces and surface tension that exists in the system when the gravity is neglected results in a differential expression of θ, the half angle of coalescence.

Polycronopoulos et al. [23] describe the steps to the solution of this problem and the quantities of interest θ and y are given by the equations 12 and 13. The differential equation in θ is solved using a Runge-Kuta algorithm with an initial value of θ, $\theta_0 = 0.01$ to avoid numerical instabilities.

$$\dot{\theta} = \frac{\Gamma}{2\sqrt{\pi}\eta r_0} \frac{[(\pi - \theta)(\cos\theta) + \sin\theta][\pi - \theta + \cos\theta\sin\theta]^{\frac{1}{2}}}{(\pi - \theta)^2 \sin\theta\tan\theta} \tag{12}$$

$$y = r_0 \frac{\sin\theta}{\sqrt{\pi - \theta + \cos\theta\sin\theta}} \tag{13}$$

In the following sections, θ and y for cylinder sintering will be referred to as θ_{cyl} and y_{cyl}

2.3. Material

The material is the 60-40 amorphous ThermaX Polyether Ketone Ketone polymer (PEKK-A) formulated by 3DXTech and made using Arkema's Kepstan [60/40 copolymer]. It is amorphous and contains only PEKK. Following the manufacturer processing parameters, the printed temperature is 325-360°C, and the chamber temperature is 70 to 150 °C. It has a glass transition temperature of 162 °C and a melting temperature of 335 °C.

2.4. Specimen Printing

The printed test specimens are created according to the 1BA Standard EN ISO 527-2 dimensions. The .STL file of the corresponding geometry was sliced into a readable G-code for an INTAMSYS funmat 610 HT printer.

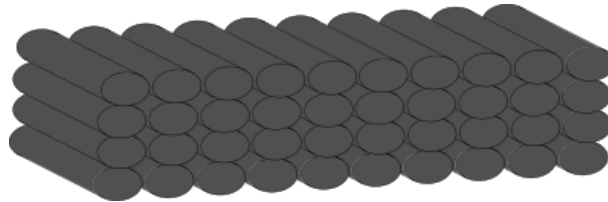The G-code path consists of superposed deposited filaments, as shown in the figure 7.

Figure 7. G-code path.

The values of the varying parameters of the Design Of Experiment (DOE) are given in Table 1. For each specified Nozzle diameter D (mm) and chamber temperature T_{inf}, a set of test pieces will be produced, resulting in nine parameter couples and samples. The layer height H of the part is given by $H = D/2$.

Other process parameters remain constant. Test pieces where printed for each varying parameter couple. For D the given nozzle diameter and T_{inf} the given chamber temperature of a test piece, the denomination $X_{T_{\text{inf}}}^{D}$ will be given to the test piece.

Table 1. Test piece DOE.

Test Piece	$X_{110}^{0.4}$	$X_{130}^{0.4}$	$X_{150}^{0.4}$	$X_{110}^{0.6}$	$X_{130}^{0.6}$	$X_{150}^{0.6}$	$X_{110}^{0.8}$	$X_{130}^{0.8}$	$X_{150}^{0.8}$
T_{inf} (°C)	110	130	150	110	130	150	110	130	150
D (mm)	0.4	0.4	0.4	0.6	0.6	0.6	0.8	0.8	0.8
H (mm)	0.2	0.2	0.2	0.3	0.3	0.3	0.4	0.4	0.4

2.5. Specimen Preparation

The test specimen were then cut in the YZ axis using an Isomet 1000 precision cutter into 6 observable surfaces,

The cut pieces of the testing specimen are cured inside a transparent KM-U resin from Presi.

The resin cylinders are then polished using a MECAPOL P200 polishing machine. The abrasive disc P180 is used to denude the surfaces of interest, then the abrasive discs P360, P840, P1000, P2400 and P4000 are used successively for 5 minutes each, with water as a suspension. Subsequently, a TOP polishing disk is applied for 5 minutes with a 6 μm Reflex LDM suspension before a RAM polishing disk with a 3μm Reflex LDM suspension.

The polishing machine head has a speed of 600 laps per minute with all disks and applies a pressure of 1.1 daN onto the polishing head. The resin cylinders are maintained immobile during the process.

2.6. Mesostructure observation

The samples are observed thanks to a VHX-7100 microscope, where two captures of each surface of interest are taken. The lighting of the scene is made by coaxial lights and is then optimized thanks to the microscope software. The images are then binarised using image processing tools.

There are 6 of such mesostructures available for each pair of chamber temperature and nozzle diameter.

The mesostructures are then cut by layers, where the longitudinal length of the voids is measured and is subtracted to the height of the layer as shown in figure 8 to obtain the longitudinal neck growth of this particular element in the layer. This operation is repeated for all voids in the layer.

In figure 8, the longitudinal neck growth is obtained by subtracting the longitudinal void length (represented in green) to the layer height (represented in orange).

The results of all the measurements are then plotted in the next section.

3. Results

The results of the various investigations are shown. It is divided in three parts, a first section were the results of the theoretical model used to predict the length of the neck between filaments are shown, a second where the experimental data measured using the microscope is displayed, and a third where the results of the two previous sections are compared. All the results are then discussed in the following section.

3.1. Theoretical longitudinal neck length

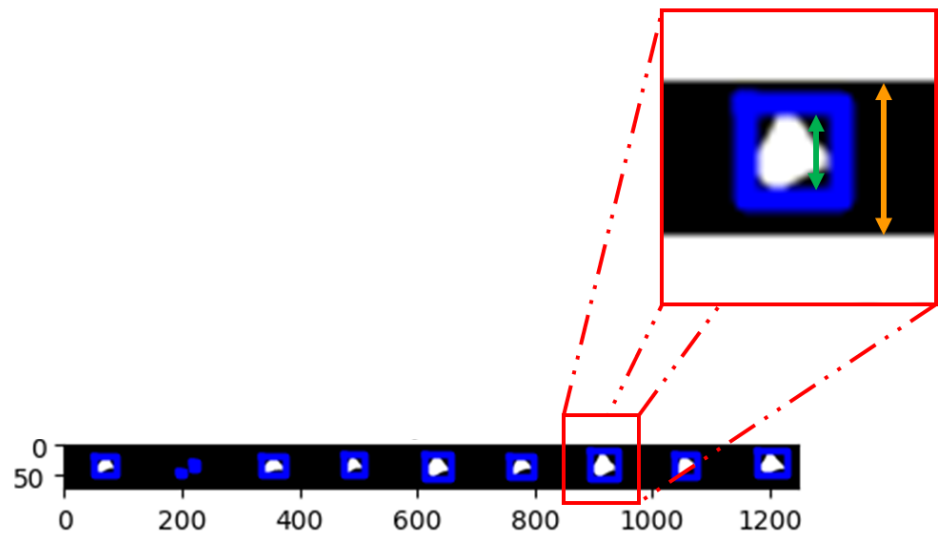Using the introduced parameters, the theoretical thermal temperature of the filament is given in figure 9:

Figure 8. Measurement of longitudinal neck growth of one coalescence occurrence in a designated layer. The color lengths are the layer height (orange) and the longitudinal void length (green).
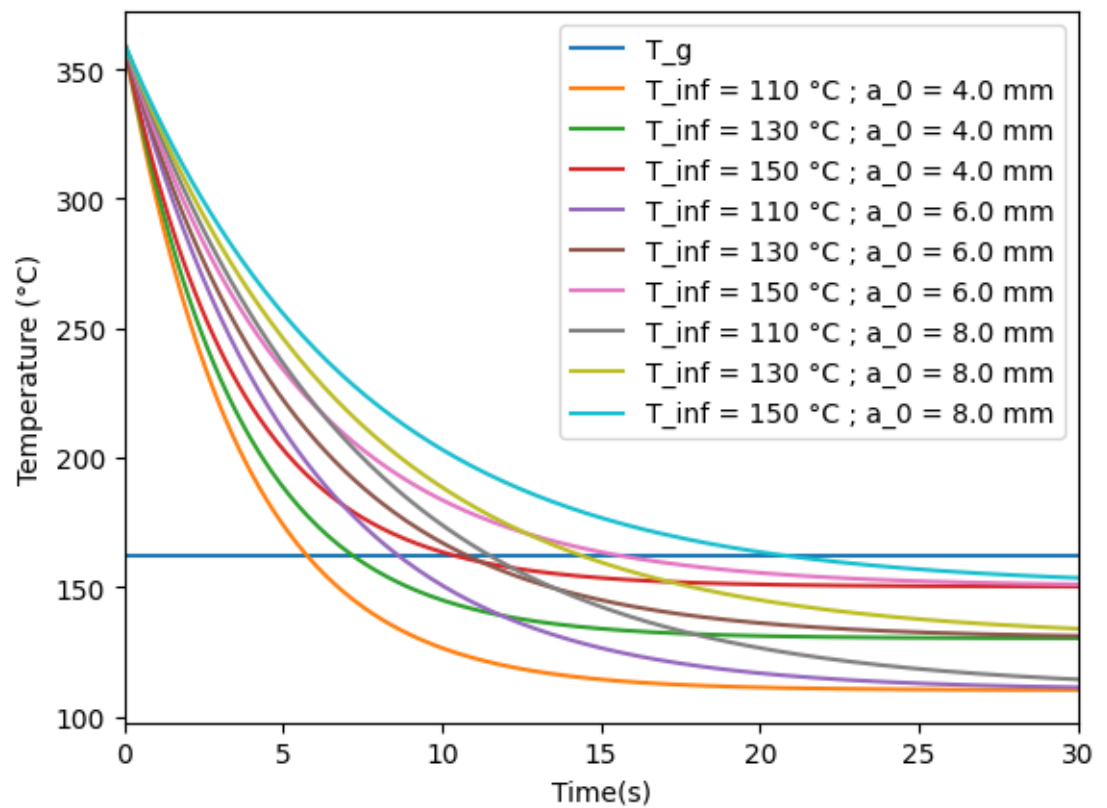

**Figure 9.** Theoretical temperature of the deposited filament

From this, the coalescence time t_c given to the polymer to form bonds in each case is obtained. It is shown as the time at which the temperature of the filament crosses the glass transition temperature in the figure 9. This coalescence time is then used as limit in the time integration to obtain the theoretical half angle θ by solving the differential equation (7) for spherical sintering and (12) for cylinder sintering. From the equations (8) and (13), the theoretical neck growth is then obtained. All the theoretical results have been compiled in the table 2.

Table 2. Theoretical results of capillary time t_c, theoretical half angle of coalescence θ_{cyl} and θ_{sph}, theoretical longitudinal neck growth y_{cyl} and y_{sph} for both spherical and cylinder sintering.

Test Piece	$X_{110}^{0.4}$	$X_{130}^{0.4}$	$X_{150}^{0.4}$	$X_{110}^{0.6}$	$X_{130}^{0.6}$	$X_{150}^{0.6}$	$X_{110}^{0.8}$	$X_{130}^{0.8}$	$X_{150}^{0.8}$
T_{inf} (°C)	110	130	150	110	130	150	110	130	150
D (mm)	0.4	0.4	0.4	0.6	0.6	0.6	0.8	0.8	0.8
H (mm)	0.2	0.2	0.2	0.3	0.3	0.3	0.4	0.4	0.4
t_c (s)	5.82	7.22	10.43	8.73	10.83	15.64	11.53	14.44	20.85
θ_{cyl} (rad)	0.26	0.3	0.35	0.35	0.39	0.43	0.41	0.45	0.49
θ_{sph} (rad)	0.18	0.22	0.27	0.28	0.33	0.38	0.36	0.4	0.45
y_{cyl} (mm)	0.13	0.15	0.17	0.26	0.29	0.32	0.41	0.44	0.48
y_{sph} (mm)	0.09	0.11	0.14	0.21	0.25	0.29	0.36	0.41	0.47

3.2. Experimental results

The pictures of the cross section of test pieces for different nozzle diameter is taken via microscope. An example of such mesostructure is shown in figure 10
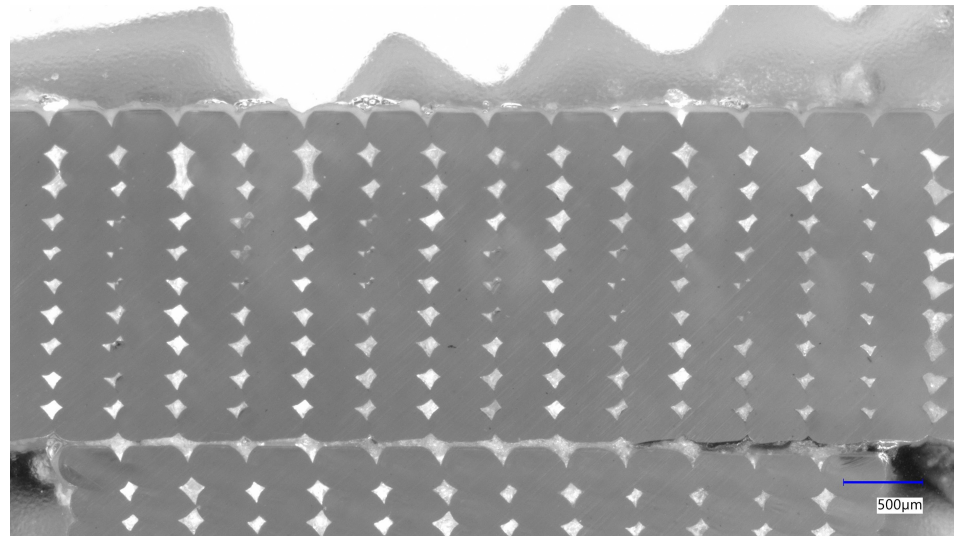
Figure 10. Microscope image for 0.4mm nozzle, 110 °C Chamber temperature : $X_{110}^{0.4}$

After image binarisation and croping, the figure 11 show the mesostructure of parts made with nozzle diameter 0.4 mm, 0.6 mm and 0.8 mm at different chamber temperatures.
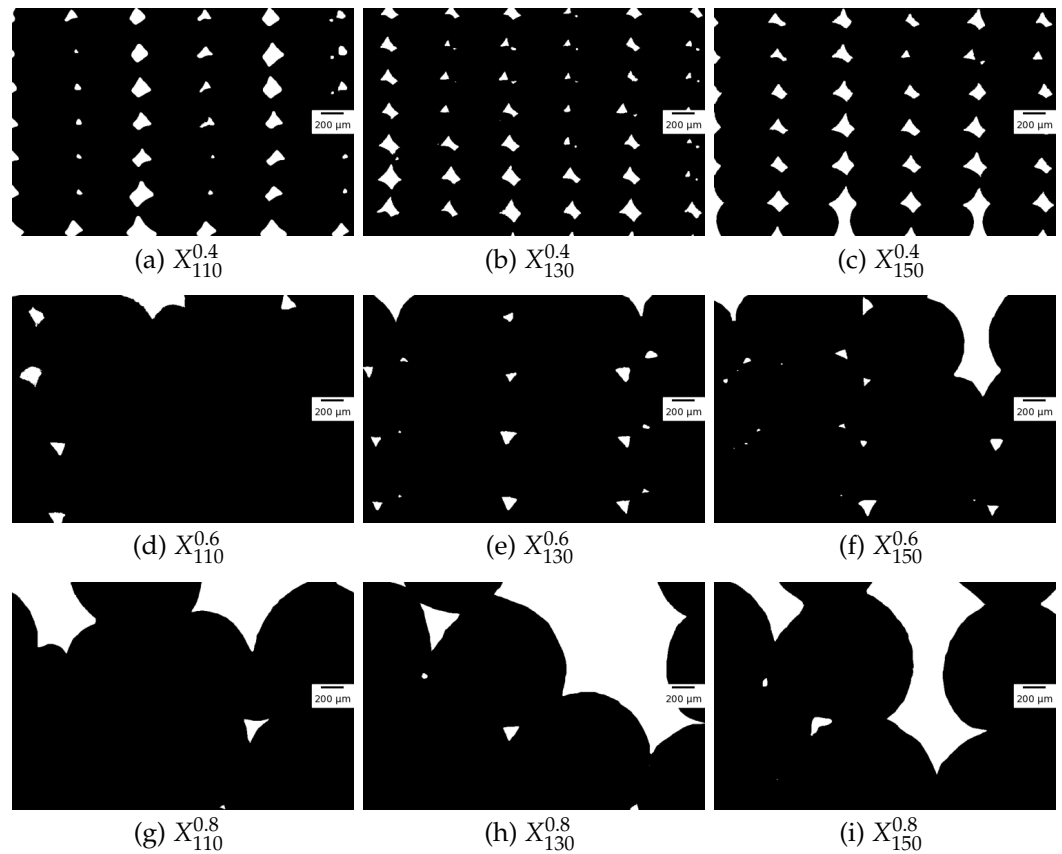
(a) $X_{110}^{0.4}$ (b) $X_{130}^{0.4}$ (c) $X_{150}^{0.4}$

(d) $X_{110}^{0.6}$ (e) $X_{130}^{0.6}$ (f) $X_{150}^{0.6}$

(g) $X_{110}^{0.8}$ (h) $X_{130}^{0.8}$ (i) $X_{150}^{0.8}$

Figure 11. Examples of mesostructures of printed test piece at different chamber temperatures T_{inf} and nozzle diameters D noted $X_{T_{\text{inf}}}^{D}$

3.3. Experimental and Theoretical Comparison

From the mesostructure, the longitudinal neck growth values are extracted as described previously, and compiled by layer and chamber temperature in figure 12 for nozzle diameter $D = 0.4$ mm and figure 13 for nozzle diameter $D = 0.6$ mm. From the shape of the porosity shown in the experimental results displayed for nozzle diameter $D = 0.8$ mm, the sintering of the part is not the principal phenomena behind the porosity of part, so the comparison with the theoretical model is not conclusive.

In the abscissa of the graphs, L is the abbreviation of Layer. It is followed by the number of the considered layer, starting with 1 for the bottom layer in contact with the raster. T is the abbreviation of Temperature, and is followed by the value of the chamber temperature corresponding to that particular print.
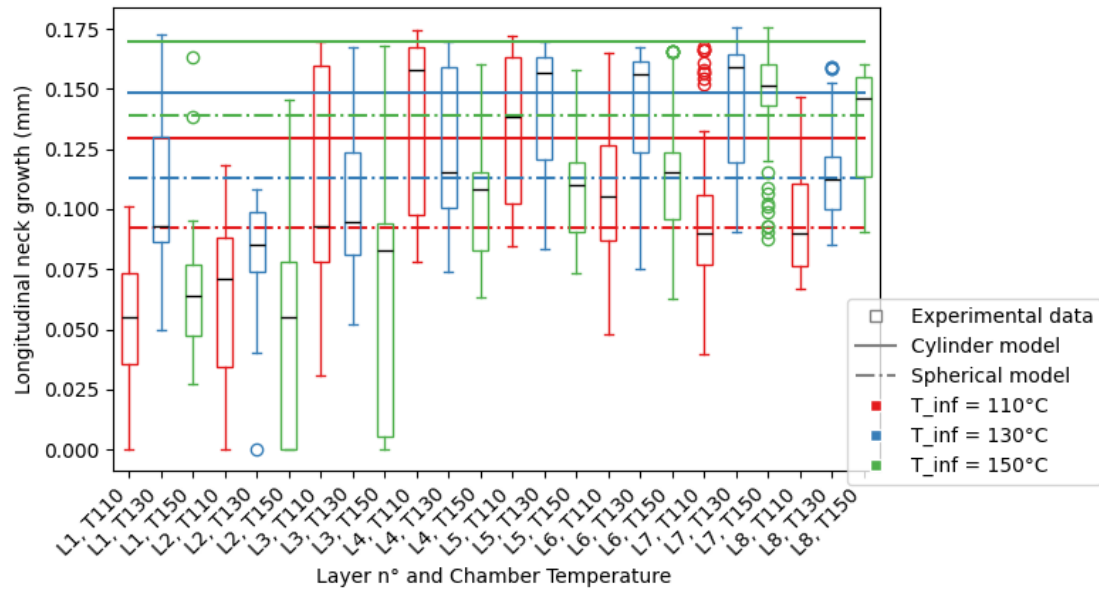
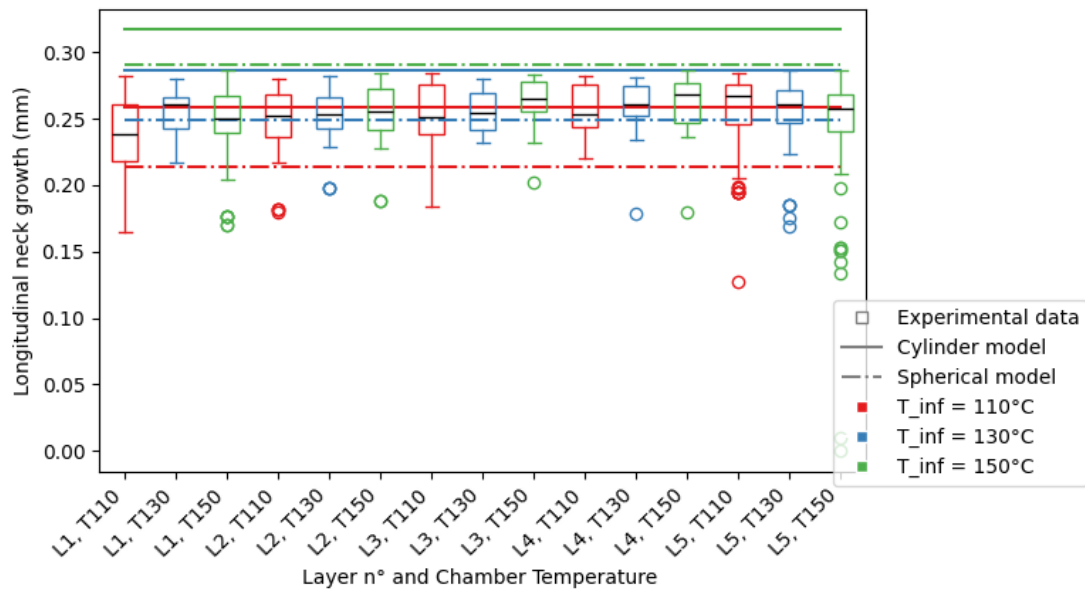**Figure 12.** Neck growth for Nozzle Diameter $D = 0.4$ mm

Figure 13. Neck growth for Nozzle Diameter $D = 0.6$ mm

In the following section, the term "theoretical longitudinal neck growth" will refer to both the cylinder and spherical modelled neck growths, representing an interval of possible neck growth measurements. The spherical calculation serves as the lower limit of the interval, and the cylinder calculation serves as the upper limit.

As shown in the previous section, the longitudinal neck growth is not the driving force behind the porosity observed for $D = 0.8$ mm, the results of the experimental measurements are not the longitudinal neck growth of the filaments. The image analysis of the printed parts with a nozzle diameter of $D = 0.8$ mm is not relevant to the comparison of the model with experimental results.

For $D = 0.4$ mm, for the first few layers, the coalescence measured is less than the theoretical value : this is due to two phenomena. Firstly, absence of contact between filaments is observed, as shown in figure 11 (c), leading to measured longitudinal neck growth equal to zero, unlike the predictions of the model. This behaviour is observed for elements printed with all chamber temperatures, but mostly for $T_{inf} = 110$ °C and $T_{inf} = 150$ °C. Secondly, the values of the non zero elements is also lower than expected, this is due to the proximity with the heating bed. The assumption that the conduction of heat through the material doesn't change its temperature is false: the substrate has similar mass to the deposited filament, hence changes in temperature in the substrate induced by the presence of the filament, and so the cooling of the material is faster than expected, leading to a lower experimental longitudinal neck growth measured than the theoretical value.

For the middle to top layers, the theoretical and the experimental estimation of the neck growth results show an overlap as the majority of experimental measurements are contained between the two boundaries defined by the models, but a large number of experimental measurement show a quasi total neck growth. This is due to the change in geometry observed in the mesostructure : the void shape going from diamonds to triangles. In the literature, occurrences of this are linked with over-extrusion as shown in Ghorbani et al. [26].

For $D = 0.6$ mm, there is contact between filaments in the first layers for all temperatures. As observed for $D = 0.4$ mm, the neck growth for the first deposited layers is reportedly smaller than that of the middle or top of the printed test piece. The observed voids are almost all triangle shaped. A complete absence of voids is also observed in several areas of the section. Large defects are also starting to appear in the top layer, leading to poor surface quality of the part, for chamber temperature $T_{inf} = 150°C$. The filaments deposited in the last layers have a rounder appearance than those deposited in the first layer, while the extrusion speed of the material has not changed.

4. Discussion

4.1. Physics analysis

This section pertains to the analysis of the physics governing the results previously displayed. Two phenomena are discussed : the first is the filament shape, and the second is the coalescence between filaments.

4.1.1. Filament shape

The model considers a perfect ellipse or sphere on which the equations of the system are solved. The experiments show that the shape of the filament is not so simple to describe. First, the nozzle is a main contributor in the shape of the deposited filament. Second, the asymmetry of the deposited filament is due to small variations in the angle of the nozzle during the printing process.

- For a nozzle diameter $D = 0.4$ mm and while the material is printed, the nozzle constrains the expansion of the material in the Z-axis by its presence. The excess material is pushed to the sides of the nozzle. As observed in the figure 11, the center of mass of the filament is higher than the middle of the filament in the Z-axis, the skinny part of the filament is at the bottom. This particular deformation is a result of the path of the nozzle, restraining the degrees of freedom of the deposited material.
  For nozzle diameter $D = 0.6$ mm, the shape of the filament show a center of mass lower than than the middle of the filament in the Z-axis, the skinny part is at the top. As stated in the previous section, the aspect of the filament is rounder for filaments at the top of the print for cooling temperature $T_{inf} = 150$ °C.
  For nozzle diameter $D = 0.8$ mm, the filaments in the first layer show little to no voids, the flow of material induced by the high printing temperature was enough to change the behaviour of the deposited filament. Higher up in the test piece, the aspect ratio of the observable filaments is near 1, meaning that the nozzle doesn't constrain the

expansion of material in the Z-axis : the substrate of the considered layer is lower than expected. A direct consequence is that the geometry of the part show defects and the mesotructure is no longer easily observable.

- Small variations in the angle of the nozzle during the deposition process result in a favored direction of flow of material. The resulting filaments show asymmetry, with the center of mass of the filament skewing to either right or left. This small change in shape may result in changes in the mesostructure of the complete test piece. This phenomena is observable for all nozzle diameters and cooling temperatures.

4.1.2. Coalescence between filaments

The coalescence between filaments varies a lot with the process parameters, and during the process, with the number of layers deposited. Here, the different types of coalescence observed are shown : absence of coalescence, coalescence resulting diamond shaped voids, coalescence resulting in triangular shaped voids, and coalescence resulting in no voids.

- For nozzle diameter $D = 0.4$ mm and cooling temperature $T = 110$ °C or $T = 150$ °C, the first layers of deposited filaments display instances of absence of coalescence. The asymmetry observed in the previous section, resulting in an absence of contact between filaments, stalls the coalescence between neighboring filaments.
- For nozzle diameter $D = 0.4$ mm, the voids can be in the shape of diamonds, formed by the coalescence of two elliptic filaments from the previous layer, and two from the current layer, meaning that the neck growth is as modelled in the theoretical part. It is nevertheless not the only type of void shape observed.
- For nozzle diameter $D = 0.4$ mm and $D = 0.6$ mm, the voids are often in the shape of triangles, meaning that the bottom left with the top right filament or top left with bottom right filament have started the sintering process, leading to two voids of smaller size and of triangular shape, or just one triangular shaped void, as one of the two disappears during the sintering process. This is due in part to the asymmetry of the deposited filaments, but also to the flow of material observed for $D = 0.6$ mm filaments. This is seen in 11 (d,e,f) as the filament bottom part is sintering with its neighbours, but the top part is not, creating the aforementioned voids, when voids are created.
- For nozzle diameter $D = 0.8$ mm, The analysis of the coalescence is not relevant as the main contributor of voids is not the coalescence but the printing defects observed that resulted from the flow of material.

4.2. Theoretical and experimental results discussion

The theoretical models are describing two flow states, between spherical, corresponding to a local sintering of the filament with its neighbour, and cylinder, corresponding to the global sintering of the whole filament length with its neighbour. The size of the zone heated by the deposition of a filament in its neighbour is the parameter that is governing the flow of material from one filament to the next. If the heated zone is small before the length of the filament, then the flow state will approach a spherical sintering (the contact with the neighboring filament changes the kinematics of the problem, the flow state is not strictly spherical). If the heated zone is comparable to the length of the filament, then the flow state will correspond to a cylinder shaped sintering. The reality is supposedly a combination of the two.

The given models may produce limits for the porosity inside a printed part, as the results for $D = 0.4$ mm and $D = 0.6$ mm show a significant overlap between the theoretical and experimental results, with both the spherical and cylinder sintering predictions acting as limits to the experimental results. There are cases where the prediction is not as precise:

- In the first layers of the print, this behaviour is changed as the conduction of the heat between the filament and the substrate is faster than expected, leading to smaller longitudinal neck growths measured.

- For $D = 0.6$ mm, the Biot number of the filament $Bi = \frac{h}{k} \frac{V}{A}$, is very similar to 0.1. The approximation giving the uniformity of the temperature in the section of the considered filament may not be verified and the actual temperature of the point of contact between filaments may be lower than modelled, leading to the over estimation of the longitudinal neck growth by the considered models.

The given models are also constant throughout the printing process and do not into account the layer number of the print, while the experimental results show clear influence of the layer number and especially in the first two deposited layers. There are also deposited filaments that have a very different aspect ratio than other filaments in the part. They are found in the higher layers of the print.

The theoretical longitudinal neck growth may be equal or greater than the layer height $H = 0.3$ mm. While the experimental neck growth is bounded by the process parameters, as the method used to measure the experimental neck growth requires a void length to be subtracted to the the layer height, it is not the case for the theoretical longitudinal neck growth. The cases where the coalescence is such that there is no void between filaments were simply not measured. The rest are represented in figure 13.

4.2.1. Impact of the cooling temperature on porosity

While the models show a clear dependence to the cooling temperature of the process, the experimental results show similar levels of mean longitudinal neck growth for all cooling temperatures. The impact of the cooling temperature on the part is mainly seen in the variations of neck growth measured between layers.

The porosity of the printed parts shows little to no variation with regards to the cooling temperature, but the model do. While it is often true that the lower the cooling temperature is, the lower the neck growth is, and the variation in neck growth is small. Still, the spherical model is better at approximating the experimental data than the cylinder model. Especially for $T_{\text{inf}} = 150$ °C, where both models predict higher values than the experimental data.

4.3. Hypothesis for the observed differences

In this section, the differences in results are explored. First, the differences between experimental results for different parameters are hypothesised. Secondly, the differences between the theoretical and experimental results are explained.

4.3.1. Differences between experimental results for the given parameters

The differences described in the previous sections can be explained thanks to a few hypothesis. The differences mentioned can be grouped by the phenomena responsible for their existence. The first group of differences is the following

- The changes in aspect ratio observed for $D = 0.6$ mm and $D = 0.8$ mm but not for $D = 0.4$ mm. The aspect ratio for the last layer for $D = 0.6$ mm and the last few layers for $D = 0.8$ mm is much closer to 1 than expected.
- When the observed aspect ratio of the filament, given by the ratio of $\frac{H}{D}$ is equal to 0.5, the position of the center of mass of the filament changes with the nozzle diameter : the higher the nozzle diameter, the lower the center of mass.

An explanation for this few differences might be that the effect of gravity on the filament and the flow of material, causing the filament to "sag". The changes in the position of the center of mass of the filament show that a force is applied to the filament and acts on the direction of the flow of material. This force is negligible for $D = 0.4$ mm but starts to affect the filament shape for $D = 0.6$ mm.

A slight variation in layer height induced by gravity, undetected by the nozzle and which compounds at each layer, may also explain the variation in aspect ratio for such filaments. With the substrate at a lower position than expected by the nozzle, the plastic deformation induced by the nozzle will be lower than for the previous layers, leading to higher chances of defects and changes in the aspect ratio of the filament.

Another set of differences can be explained thanks to the preferred direction of the flow of material from the nozzle, induced by a slight angling defect of the nozzle :

- The coalescence of filaments from different layers that are not directly above one another that occurs systematically for $D \geq 0.6$ mm, and often for $D = 0.4$ mm.
- the lack of coalescence between filaments observed in the first few layers for $D = 0.4$ mm.

As the nozzle isn't completely parallel to the build plate, a small angle defect will impact the direction of the flow of filaments, skewing the position of filament center toward the sides, and creating absence of coalescence in between neighboring filaments. In the case for coalescence between filaments that should not be in contact, the changes in geometry induced by this slight defect create now neighboring filaments to coalesce with, impacting the voids' shape and length.

The last set of differences seen, is pertaining to :

- the value of the longitudinal neck growth for non zero elements of the first few layers lower than expected.
- the changes observed for the longitudinal neck growth for different layers of the printed test piece.

This last set of differences is explained thanks to the changes in conduction that occur during the build of the part. In the first layers, the heated zone of the substrate by the filament may be longer than the substrate itself. But the printing bed cools the material to a given value, making the filament cool faster than expected, as the heat given to the substrate is absorbed by the printing bed. After the first few layers, a plateau is reached and the longitudinal neck growth of the following layers show less variation, once the zone heated by the filament is farther away from the printing bed.

4.3.2. Limits of the models

The models, either describing the sintering of spheres or cylinders, are able to give an approximation of the values of the measured longitudinal neck growth of a print when compared with compatible data, but they are not able to account for all experimental variations.

This approximation is sometimes too high. This can be explained by the combination of two factors :

- for $D = 0.6$ mm, the variation in temperature resulting in the variation of the model prediction to values around and above the layer height of the print $H = 0.3$ mm. It is not represented in the experimental data because of the absence of voids for a large part of the observed section, resulting in no longitudinal neck growth to compare the model prediction to.
- the temperature inside a filament is not entirely constant, so the temperature at the points for contact may be lower than modelled, leading to smaller longitudinal neck growth measured.

Still, the majority of measurements of the neck growth is comprised between the upper limit given by the modelling of the sintering of cylinders, and the lower limit given by the modelling of the sintering of spheres.

The variations of the longitudinal neck growth between layers is also not shown by the models, as the variations induced by the proximity of the printing bed and the detected aspect ratio variations are not studied. In general, unexpected experimental variations are not predicted by the model.

The variations in theoretical longitudinal neck growth recorded when varying the cooling temperature of the print are not measured experimentally. The experimental longitudinal neck growth show little variation in absolute value with the cooling temperature, but there is variation in the layer number where the maximum longitudinal neck growth is recorded.

5. Conclusion

A numerical model of the coalescence between filament was applied to PEKK for larger filaments diameter than available in the literature. The impact of the nozzle diameter and chamber temperature on the longitudinal neck growth was measured using to image analysis. The mesostructure variation observed were discussed and the differences with the numerical model explained, furthering knowledge of high performance polymer parts behaviour made by Fused Filament Fabrication. The following conclusions are given :

- While the order of magnitude of the model is correct, the experimental nature of fused filament fabrication leads to a high disparity in neck growths inside a single layer, leading also a to disparity in void size between layers.
- When the shape of the void is in accordance with the model, the model is usable to obtain a quantitative approximation of the longitudinal neck growth knowing the printing parameters. The instances where the shape of the void is not in accordance to the model are when absence of contact between filaments is observed, or when the voids are not in the shape of diamonds as shown in figure 11.
- While in a perfect environment, the impact of the nozzle diameter will easily be explained thanks to the equations (12) and (7). The plastic deformation of the filament by the nozzle changes the geometry of the filament, leading to disparities between the theoretical model and the experimental measures.
- The spherical model acts as the upper boundary of the porosity inside a part. As the porosity of a part is limited, a conservative approach to the calculation of the neck growth results in higher porosity of part, leading to stricter security margins as discussed previously in the comparison between experimental and theoretical neck growth and shown in figures 12 and 13.

To further the prediction of the effect of chamber temperature and nozzle diameter on the longitudinal neck growth, a complete study in computational fluid dynamics should be carried with the goal of solving the Navier Stokes equation of the coalescence of two adjacent filaments to compare to the experimental data, and should validate the approximations used in the model.

A model of the neck growth of triangle shaped voids should be added to the model to predict the neck growth in the test piece when relevant. A diagnostic of when to use diamond of triangle shaped void should be added to the model.

To link the porosity of the part to its mechanical behaviour, mechanical testing should be conducted. Then a framework from printing parameter to porosity to mechanical behaviour will be available for use.

Institutional Review Board Statement: Not applicable

Informed Consent Statement: Not applicable

Data Availability Statement: Data available upon request

Conflicts of Interest: The authors declare no conflicts of interest. The funders had no role in the design of the study; in the collection, analyses, or interpretation of data; in the writing of the manuscript; or in the decision to publish the results.

Abbreviations

The following abbreviations are used in this manuscript:

FFF	Fused Filament Fabrication
PAEK	Polyaryletherketone
PEKK	Polyether ketone ketone
PEEK	Polyether ether ketone
Bi	Biot number
H	Layer height
D	Nozzle diameter
T_{inf}	Cooling temperature (bed and ambient)
t_c	coalescence time
θ_{cyl}	theoretical half angle of coalescence for cylinder based modelling
θ_{sph}	theoretical half angle of coalescence for spherical modelling
y_{cyl}	theoretical longitudinal neck growth for cylinder based modelling
y_{sph}	theoretical longitudinal neck growth for spherical modelling
T_g	Glass transition temperature of PEKK-A
PEKK-A	amorphous PolyEther Ketone Ketone polymer
°C	degree Celsius
a_0	initial radius of sphere
a	in 2.2.1 : radius of sphere during coalescence, in 2.2.2 : semi-major axis of elliptic cylinder
a_f	radius of sphere after coalescence
S	area of section of two spheres during coalescence
W_V	Work of viscosity forces
W_S	Work of surface tension
r_0	initial radius of circular cylinder built from elliptic cylinder
b	semi-minor axis of elliptic cylinder

References

1. Pereira, T.; Kennedy, J.V.; Potgieter, J. A comparison of traditional manufacturing vs additive manufacturing, the best method for the job. *Procedia Manufacturing* **2019**, *30*, 11–18. https://doi.org/10.1016/j.promfg.2019.02.003.
2. Rajaguru, K.; Karthikeyan, T.; Vijayan, V. Additive manufacturing – State of art. *Materials Today: Proceedings* **2020**, *21*, 628–633. https://doi.org/10.1016/j.matpr.2019.06.728.
3. Ahmadifar, M.; Benfriha, K.; Shirinbayan, M.; Tcharkhtchi, A. Additive Manufacturing of Polymer-Based Composites Using Fused Filament Fabrication (FFF): a Review. *Applied Composite Materials* **2021**, *28*, 1335–1380. https://doi.org/10.1007/s10443-021-09933-8.
4. Bikas, H.; Stavropoulos, P.; Chryssolouris, G. Additive manufacturing methods and modelling approaches: a critical review. *The International Journal of Advanced Manufacturing Technology* **2016**, *83*, 389–405. https://doi.org/10.1007/s00170-015-7576-2.
5. Popescu, D.; Zapciu, A.; Amza, C.; Baciu, F.; Marinescu, R. FDM process parameters influence over the mechanical properties of polymer specimens: A review. *Polymer Testing* **2018**, *69*, 157–166. https://doi.org/10.1016/j.polymertesting.2018.05.020.
6. Nachal, N.; Moses, J.A.; Karthik, P.; Anandharamakrishnan, C. Applications of 3D Printing in Food Processing. *Food Engineering Reviews* **2019**, *11*, 123–141. https://doi.org/10.1007/s12393-019-09199-8.
7. Ranasinghe, K.; Sabatini, R.; Gardi, A.; Bijjahalli, S.; Kapoor, R.; Fahey, T.; Thangavel, K. Advances in Integrated System Health Management for mission-essential and safety-critical aerospace applications. *Progress in Aerospace Sciences* **2022**, *128*, 100758. https://doi.org/10.1016/j.paerosci.2021.100758.
8. Huang, S.H.; Liu, P.; Mokasdar, A.; Hou, L. Additive manufacturing and its societal impact: a literature review. *The International Journal of Advanced Manufacturing Technology* **2013**, *67*, 1191–1203. https://doi.org/10.1007/s00170-012-4558-5.
9. Wong, K.V.; Hernandez, A. A Review of Additive Manufacturing. *International Scholarly Research Notices* **2012**, *2012*, e208760. Publisher: Hindawi, https://doi.org/10.5402/2012/208760.
10. Fu, X.; Lin, Y.; Yue, X.J.; XunMa.; Hur, B.; Yue, X.Z. A Review of Additive Manufacturing (3D Printing) in Aerospace: Technology, Materials, Applications, and Challenges. In Proceedings of the Mobile Wireless Middleware, Operating Systems and Applications; Tang, D.; Zhong, J.; Zhou, D., Eds., Cham, 2022; EAI/Springer Innovations in Communication and Computing, pp. 73–98. https://doi.org/10.1007/978-3-030-98671-1_6.

11. Tao, Y.; Kong, F.; Li, Z.; Zhang, J.; Zhao, X.; Yin, Q.; Xing, D.; Li, P. A review on voids of 3D printed parts by fused filament fabrication. *Journal of Materials Research and Technology* **2021**, *15*, 4860–4879. https://doi.org/10.1016/j.jmrt.2021.10.108.

12. Das, A.; Chatham, C.A.; Fallon, J.J.; Zawaski, C.E.; Gilmer, E.L.; Williams, C.B.; Bortner, M.J. Current understanding and challenges in high temperature additive manufacturing of engineering thermoplastic polymers. *Additive Manufacturing* **2020**, *34*, 101218. https://doi.org/https://doi.org/10.1016/j.addma.2020.101218.

13. Zawaski, C.; Williams, C. Design of a low-cost, high-temperature inverted build environment to enable desktop-scale additive manufacturing of performance polymers. *Additive Manufacturing* **2020**, *33*, 101111. https://doi.org/10.1016/j.addma.2020.101111.

14. Rashid, A.A.; Koç, M. Fused Filament Fabrication Process: A Review of Numerical Simulation Techniques. *Polymers* **2021**, *13*, 3534. Number: 20 Publisher: Multidisciplinary Digital Publishing Institute, https://doi.org/10.3390/polym13203534.

15. Sun, Q.; Rizvi, G.; Bellehumeur, C.; Gu, P. Effect of processing conditions on the bonding quality of FDM polymer filaments. *Rapid Prototyping Journal* **2008**, *14*, 72–80. Publisher: Emerald Group Publishing Limited, https://doi.org/10.1108/13552540810862028.

16. Bellehumeur, C.; Li, L.; Sun, Q.; Gu, P. Modeling of Bond Formation Between Polymer Filaments in the Fused Deposition Modeling Process. *Journal of Manufacturing Processes* **2004**, *6*, 170–178. https://doi.org/10.1016/S1526-6125(04)70071-7.

17. Pokluda, O.; Bellehumeur, C.T.; Vlachopoulos, J. Modification of Frenkel's model for sintering. *AIChE Journal* **1997**, *43*, 3253–3256. _eprint: https://onlinelibrary.wiley.com/doi/pdf/10.1002/aic.690431213, https://doi.org/10.1002/aic.690431213.

18. Shahriar, B.B.; France, C.; Valerie, N.; Arthur, C.; Christian, G. Toward improvement of the properties of parts manufactured by FFF (fused filament fabrication) through understanding the influence of temperature and rheological behaviour on the coalescence phenomenon. *AIP Conference Proceedings* **2017**, *1896*, 040008. https://doi.org/10.1063/1.5008034.

19. Lepoivre, A.; Levy, A.; Boyard, N.; Gaudefroy, V.; Sobotka, V. Coalescence in fused filament fabrication process: Thermo-dependent characterization of high-performance polymer properties. *Polymer Testing* **2021**, *98*, 107096. https://doi.org/10.1016/j.polymertesting.2021.107096.

20. Jiang, S.; Yun, C.; Huang, X.; Zhao, C. Investigation on the Forming Process of Polylactic Acid in Material Extrusion Additive Manufacturing Technique, 2023. https://doi.org/10.2139/ssrn.4516996.

21. Fang, L.; Yan, Y.; Agarwal, O.; Yao, S.; Seppala, J.E.; Kang, S.H. Effects of Environmental Temperature and Humidity on the Geometry and Strength of Polycarbonate Specimens Prepared by Fused Filament Fabrication. *Materials* **2020**, *13*, 4414. Number: 19 Publisher: Multidisciplinary Digital Publishing Institute, https://doi.org/10.3390/ma13194414.

22. Bhalodi, D.; Zalavadiya, K.; Gurrala, P.K. Influence of temperature on polymer parts manufactured by fused deposition modeling process. *Journal of the Brazilian Society of Mechanical Sciences and Engineering* **2019**, *41*, 113. https://doi.org/10.1007/s40430-019-1616-z.

23. Polychronopoulos, N.D.; Vlachopoulos, J. The role of heating and cooling in viscous sintering of pairs of spheres and pairs of cylinders. *Rapid Prototyping Journal* **2020**, *26*, 719–726. Publisher: Emerald Publishing Limited, https://doi.org/10.1108/RPJ-06-2019-0162.

24. Jiang, S.; Yun, C.; Ying, H.; Chen, J.; Zhao, C.; Yao, H. Investigation on the forming process of polylactic acid in material extrusion additive manufacturing technique. *International Journal of Material Forming* **2024**, *17*, 27. https://doi.org/10.1007/s12289-024-01828-w.

25. Weisstein, E.W. Circular Segment. *From MathWorld–A Wolfram Web Resource. https://mathworld.wolfram.com/CircularSegment.html*.

26. Ghorbani, J.; Koirala, P.; Shen, Y.L.; Tehrani, M. Eliminating voids and reducing mechanical anisotropy in fused filament fabrication parts by adjusting the filament extrusion rate. *Journal of Manufacturing Processes* **2022**, *80*, 651–658. https://doi.org/10.1016/j.jmapro.2022.06.026.